Hindawi
Advances in Materials Science and Engineering
Volume 2023, Article ID 9847204, 1 page
https://doi.org/10.1155/2023/9847204

Retraction

Retracted: Interfacial Transport Study of Ultra-Thin InN-Enhanced Quantum Dot Solar Cells

Advances in Materials Science and Engineering

Received 26 September 2023; Accepted 26 September 2023; Published 27 September 2023

This article has been retracted by Hindawi following an investigation undertaken by the publisher [1]. This investigation has uncovered evidence of one or more of the following indicators of systematic manipulation of the publication process:

(1) Discrepancies in scope

(2) Discrepancies in the description of the research reported

(3) Discrepancies between the availability of data and the research described

(4) Inappropriate citations

(5) Incoherent, meaningless and/or irrelevant content included in the article

(6) Peer-review manipulation

The presence of these indicators undermines our confidence in the integrity of the article's content and we cannot, therefore, vouch for its reliability. Please note that this notice is intended solely to alert readers that the content of this article is unreliable. We have not investigated whether authors were aware of or involved in the systematic manipulation of the publication process.

Wiley and Hindawi regrets that the usual quality checks did not identify these issues before publication and have since put additional measures in place to safeguard research integrity.

We wish to credit our own Research Integrity and Research Publishing teams and anonymous and named external researchers and research integrity experts for contributing to this investigation.

The corresponding author, as the representative of all authors, has been given the opportunity to register their agreement or disagreement to this retraction. We have kept a record of any response received.

References

[1] S. Wang, D. Zhang, and Z. Ju, "Interfacial Transport Study of Ultra-Thin InN-Enhanced Quantum Dot Solar Cells," *Advances in Materials Science and Engineering*, vol. 2022, Article ID 5862204, 10 pages, 2022.

Hindawi
Advances in Materials Science and Engineering
Volume 2022, Article ID 5862204, 10 pages
https://doi.org/10.1155/2022/5862204

Research Article

Interfacial Transport Study of Ultra-Thin InN-Enhanced Quantum Dot Solar Cells

Shuaijie Wang, Dong Zhang, and Zhenhe Ju

School of Renewable Energy, Shenyang Institute of Engineering, Shenyang 110136, China

Correspondence should be addressed to Shuaijie Wang; d11402027@mail.dlut.edu.cn

Received 11 May 2022; Accepted 13 June 2022; Published 7 July 2022

Academic Editor: Ravi Samikannu

For human society, all activities require energy support. Solar cells are a means of converting solar energy into electrical energy using the photovoltaic effect of semiconductor materials. This photoelectric absorber layer has been developed for more than 70 years. Currently, the layered solar panel industry has achieved an energy conversion efficiency of 47%. In addition to efficiency, the cost of solar cells has been optimized, and the cost of commercial silicon solar cells has been greatly reduced. There is an urgent need for energy transfer research through the solar cell interface. Many researchers are studying and discovering new elements in this field. On this basis, the transmission ion interface of ultra-thin in-amplified quantum solar cell panels was studied, and very effective conclusions were drawn on the basis of experimental preparation and analysis.

1. Introduction

Energy is the basis of all activities, the guarantee for the smooth functioning of the physical world, and the backbone force that supports the development of human society. For human society, all activities require the support of energy [1]. In the period of fuel wood energy, people's demand and use of energy were relatively limited, mainly using wood, grass, and other energy sources to boil water and cook [2]. During the fossil energy period, people used coal, oil, natural gas, etc., to power the development of society.

To this day, fossil energy continues to provide us with energy as a major part of the human energy mix. Figure 1 shows the findings on the share of all forms of energy in total energy consumption at the global scale in 2017, which shows that fossil energy accounts for 79.7% of the current global energy supply [3].

Fossil energy has supported the human society through the first and second industrial revolutions and has made an indelible contribution to the development of human society. As society's demand for energy has gradually increased, the use of fossil energy has also increased [4]. However, since the formation of fossil energy requires a long process, the total amount of fossil energy is basically not increasing, which leads to the gradual decrease of fossil energy available to human beings and the imminent crisis of running out of fossil energy. According to the world energy statistical yearbook, even coal, the largest remaining resource, will be depleted in 132 years according to the current usage, while oil and natural gas can only support human use for another 50 years, as shown in Figure 2 [5]. Without energy, the development of human society will come to a halt or even regress back to the slash-and-burn period. Therefore, for the continuity of human development, new energy sources that can replace fossil energy sources need to be developed urgently.

After a long period of unremitting efforts, a series of new energy have been developed and utilized by people. Compared with fossil energy, these new forms of energy have significant advantages in terms of environmental friendliness and sustainable utilization. Solar energy is the energy radiated to the outside world by the sun through thermonuclear fusion, which has the characteristics of large total energy, long availability, uniform distribution, and no pollution, and is an extremely ideal energy source.

But this economy is an economy based on fossil energy sources, and once fossil energy sources face depletion, the

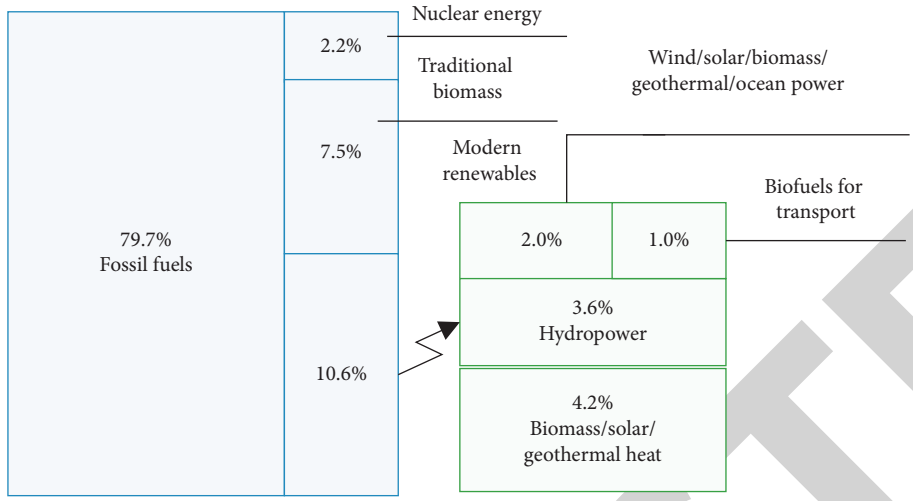

Figure 1: Share of various forms of energy in total energy consumption at the global scale in 2017.

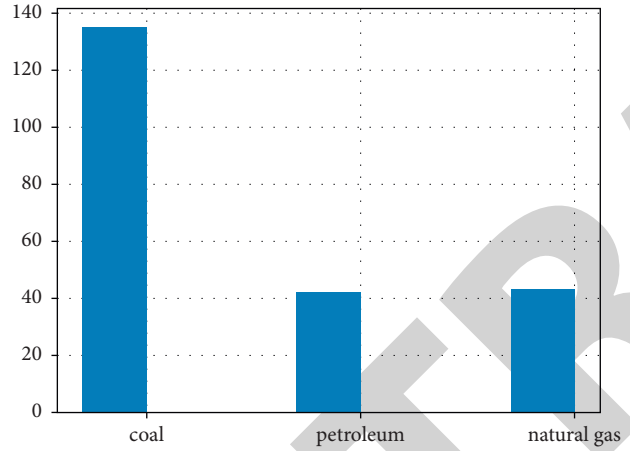

Figure 2: Global fossil fuel storage and production ratio histogram in 2019.

human economy will face heavy damage. The three global oil crises, for example, have had a serious impact on the global economy. According to the rate and trend of global fossil energy consumption, the most optimistic estimate of the American Petroleum Association (APA) is that the fossil energy reserves will only last for more than 100 years [6]. On the other hand, the extraction and use of oil and coal have simultaneously caused irreparable damage to the Earth's environment, most typically in the form of atmospheric pollution and the greenhouse effect. The scientific and orderly exploitation of nuclear energy and natural resources (e.g., wind, solar, hydro, etc.) can effectively improve these problems in light of current human science and technology [7]. At the beginning of 2011, nuclear energy was considered to be at the beginning of a renaissance, but with the Fukushima nuclear accident, the brakes were applied sharply. The development and utilization of solar energy, the most abundant of natural energy sources, has now long been a new field of research worldwide, and initial progress has been made in the collection, storage, and utilization of solar energy.

2. Related Work

Photothermal utilization and photovoltaic utilization are the two main forms of solar energy utilization by humans at present. Photothermal utilization refers to the use of material molecules, converting light energy into heat energy to be utilized. Photovoltaic utilization refers to the use of solar cell devices to convert the energy carried by sun photons into the potential energy of electrons in semiconductor materials and transport it outward. Compared to the photovoltaic utilization of solar energy, photothermal utilization is inefficient because the conversion process requires the participation of a medium [8].

The beginning of solar cells was the discovery of the photovoltaic effect by the French physicist Becquerel in 1839, and the discovery of this effect made the emergence of solar cells possible. In 1905, Albert Einstein proposed the photoelectric effect to explain the phenomenon of electrons emitted by materials exposed to light, and this theory was the basis for the work on solar cells. In the 1950s, PN junctions were prepared by wafers, and a significant photovoltaic effect was found in these PN junctions. With the photovoltaic effect of this PN junction, Bell Laboratories prepared solar cells with 4.5% photovoltaic conversion efficiency, which was later increased to 6% [9]. In the following decades, the performance of solar cells has been continuously improved and the types of solar cells have been enriched [10]. Among them, silicon-based solar cells have the longest history of development and have achieved excellent results both in terms of high-efficiency devices and commercialized modules [11]. Based on the excellent light absorption ability of these new photovoltaic materials, only a few hundred nanometers to a few microns of light absorption layer material are needed to achieve complete absorption of sunlight, which makes the preparation of solar cell devices requires only a very small amount of material, significantly reducing the material cost of device fabrication, thus making this type of solar cell power generation [12]. This reduces the material cost for device fabrication and, thus the cost of power generation for this type of solar cell.

Table 1: Classification of solar cells.

Classification	Category	Efficiency (%)	Cost	Advantages and disadvantages
Silicon crystalline solar cells (first generation)	Monocrystalline Silicon	27.5	very high	Complex process, good stability
	Polysilicon	23.3	Higher	Simple process, high development potential
	Amorphous Silicon	21.5	High	Simple process, poor stability
Thin film solar cells (second generation)	Cadmium Telluride (CdTe)	22.3	Lower	Serious environmental pollution
	Gallium Arsenide (GaAs)	27.9	very high	Good stability
	Copper Indium Gallium Selenide (CIGS)	23.3	Higher	Shortage of raw materials for preparation
	Inorganic Cell (CZTSSe)	12.5	Low	Simple process, poor stability
New concept solar cells (third generation)	Dye Sensitization (DSSC)	12.3	Lower	Severe pollution, poor stability
	Quantum dot sensitization (QDSC)	16.7	Low	Low efficiency, good stability
	Calcium Titanite (PSCs)	25.1	Low	Simple process, poor stability

Although the cost of these solar cells has dropped significantly, they are still more expensive than the current thermal power generation and are at a disadvantage in competition with thermal power generation [13]. For example, the maximum capacity of copper indium gallium selenide solar cells is limited by the presence of rare metals indium and gallium in the material, while cadmium telluride solar cells need to consider the possible loss of heavy metal cadmium to the natural environment during the process of use [14]. They mostly use organic materials to construct the devices, and the more representative ones are organic small-molecule solar cells using organic small-molecule materials as the donor and receptor [15]. The new solar cells have the characteristics of little or no pollution to the environment and low material requirement, and also their photoelectric conversion efficiency can be accepted [16–18].

According to the time of its appearance in the market, the development of solar cell technology was divided into three generations by Martin Green, a well-known expert [19]. Table 1 specifies information on the categories, current efficiencies, preparation costs, and advantages and disadvantages of several types of solar cells.

Based on the analysis of the three generations of solar cells, the efficiency of the new chalcogenide solar cells is very close to that of the traditional monocrystalline silicon and gallium arsenide solar cells and has a lower manufacturing cost and process compared to them, thus becoming one of the most popular categories in the solar cell research field in recent years [20].

3. Basic Knowledge

The working principle of solar cell is mainly divided into three processes: light absorption process, electron-hole pair excitation process, and photogenerated carrier separation process. As in Figure 3, firstly, electron-hole pairs are generated when sunlight irradiates on the PN junction sample of the semiconductor, and secondly, the electron-hole pairs generated are transferred.

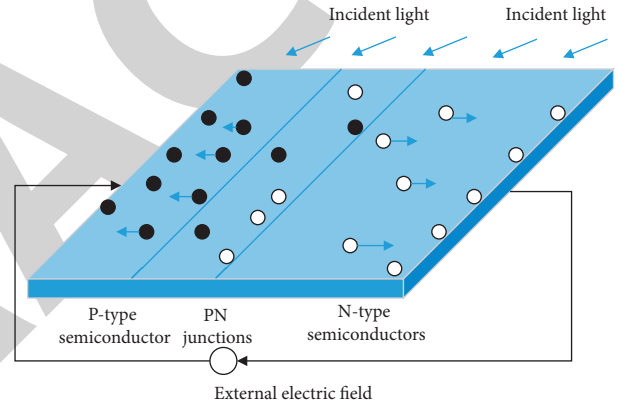

Figure 3: Working principle of solar cell.

3.1. Characteristics and Parameters of Solar Cells. The voltammetric characteristic curve is a function of the current I (Current, A) and voltage V (Voltage, V) under certain light intensity and ambient temperature, as shown in Figure 4. Since the magnitude of the current is affected by the solar cell area A (solar cell area, cm^2), the current density J (current density, A/cm^2) is commonly used instead of the current I to describe the voltammetric characteristics. The relationship between the two is $J = I/A$; that is, the size of the current I is proportional to the area of the solar cell.

For the solar cell Ohm's law, if the load resistance R (load resistance, Ω) is added, the formula is $J = V/AR$. Figure 4 shows the correspondence between the size of the load resistance and the operating current and voltage ($R_1 > R_2 > R_3$).

The photovoltaic conversion efficiency (IPCE), energy conversion efficiency (PCE), maximum output power (maximum output power, P_{max}), fill factors (fill factors, FF), energy conversion efficiency (power conversion efficiency, PCE), and other components are the values of these parameters that measure the good and bad of solar cells.

The definition of each parameter and the influencing factors are as follows.

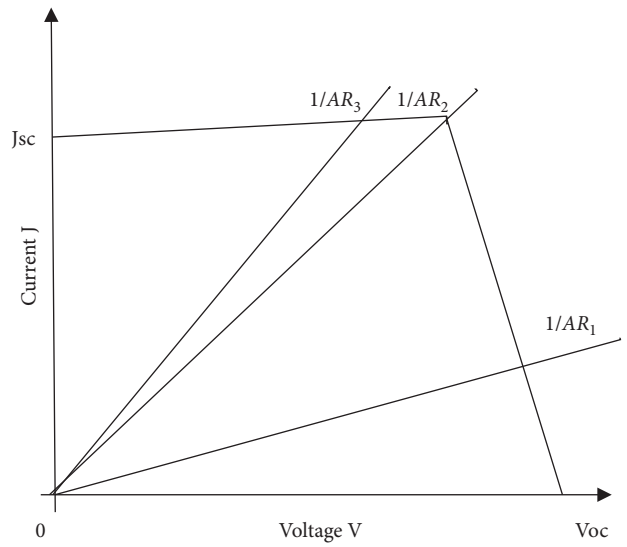

Figure 4: Solar cell voltammetric characteristic curve.

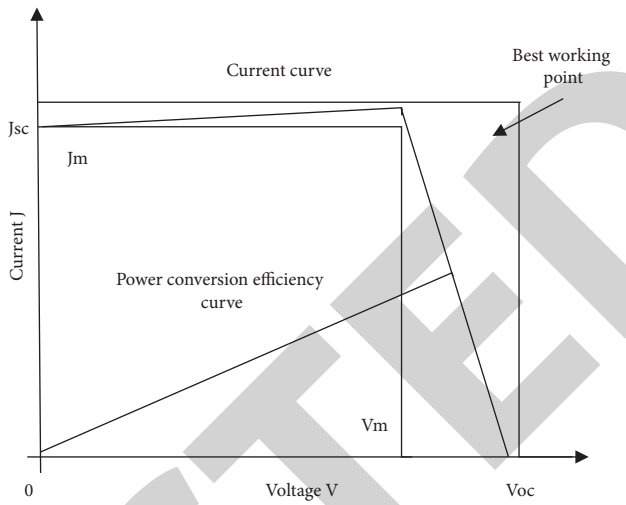

Figure 5: Voltammetric characteristic curve of the solar cell.

3.1.1. Open-Circuit Voltage V_{oc}. In the voltammetric characteristic curve is expressed as the intercept of the curve on the voltage axis shown in Figure 4. The V_{oc} size of solar cells is largely determined by the energy. In addition, different cell structures, different absorber layer materials, interface properties, and the degree of charge compounding in the device.

3.1.2. Short-Circuit Current Density J_{sc}. In the voltammetric characteristic curve is expressed as the intercept of the curve on the current density axis shown in Figure 4. There are various factors affecting the short-circuit current, including light intensity, cell structure, thickness of different layer materials, the nature of carrier transport, and the type of absorber layer material. The smaller the band gap of the absorber layer material, the greater the absorption spectrum can match the solar spectrum so that more photons can be converted into electricity.

The short-circuit current J_{sc} with IPCE and the solar photon flux, whose integral equation is shown in the following equation:

$$J_{ph} = J_{sc} = q\int_0^{\infty} QE(E)b_s(E,T_s)\mathrm{d}E. \quad (1)$$

It indicates the number of solar radiation photons per unit time, area energy in the range of E to $E + dE$, $b_s(E,T_s)$, and the temperature of the sun T_s related.

3.1.3. Photovoltaic Conversion Efficiency (IPCE). Photovoltaic conversion efficiency (IPCE) is a measure of the efficiency of incident light energy to solar cells after the final conversion into electricity, which is usually used as the EQE. The EQE is usually used as the index of IPCE. The defining equation is shown in the following equation:

$$\mathrm{IPCE}(\%) = \frac{n_e}{n_p} = \frac{1240 \times J_{SC}}{\lambda \times P_{in}} \times 100\%, \quad (2)$$

where λ denotes the wavelength of incident monochromatic light and P_{in} denotes the incident light power.

The photovoltaic conversion efficiency of solar cells generally depends on the following three factors.

(1) The absorption efficiency of the material for photons;

(2) The separation efficiency of the carriers;

(3) Carrier transport efficiency.

In addition, its value is also related to the wavelength or energy of light.

3.1.4. Maximum Output Power $P_{\max}$. The maximum output power $P_{\max}$, that is, in a certain load resistance R, the output of the product of operating current and operating voltage can reach the maximum value, also known as rated power (rated power density), in the voltammetric characteristic curve shown in Figure 5 is called the best working point, respectively, expressed in V_{mp}, J_{mp}.

3.1.5. Filling Factor FF. The defining equation is shown in the following equation:

$$\mathrm{FF} = \frac{P_{\max}}{V_{oc} \times J_{sc}} = \frac{V_{mp} \times J_{mp}}{V_{oc} \times J_{sc}}. \quad (3)$$

In Figure 5, the area of the rectangle corresponding to the optimal operating point $P_{\max} = V_{mp} \times J_{mp}$. The series and parallel resistance of the solar cell device has a large impact on *FF*. The smaller the parallel resistance of the device, the higher the shunt current.

3.1.6. Energy Conversion Efficiency PCE. The defining equation and its relationship are shown in the following equation:

$$\mathrm{PCE} = \frac{P_{\max}}{P_{in}} = \frac{V_{mp}, J_{mp}}{P_{in}} = \frac{FF \times V_{oc} \times J_{sc}}{P_{in}}. \quad (4)$$

Table 2: Performance parameters statistics of some different types of solar cells.

Battery type	Bandgap Eg (eV)	Cell area (A/cm^2)	V_{OC}/V	$J_{SC}/(\mathrm{mA/m^2})$	FF (%)	PCE (%)
Monocrystalline Silicon	1.13	79.1	0.739	42.66	84.91	26.8
Cadmium Telluride (CdTe)	1.45	1.0624	0.8760	30.26	79.5	21.1
Gallium Arsenide (GaAs)	1.43	0.997	1.1271	29.77	86.6	29.0
Copper Indium Gallium Selenide (CIGS)	1.20	1.042	0.732	39.57	80.3	23.34
CZTS	—	1.112	0.7085	21.79	65.2	10.1
Dye Sensitization (DSSC)	—	1.004	0.745	22.49	68.8	13.47
Organic Cells	—	1.025	0.8423	23.27	68.5	13.47
Calcium Titanite (PSCs)	~1.5	1.0236	1.194	21.65	83.7	21.4

The energy conversion efficiency curve is shown in Figure 5. Since energy conversion efficiency is closely related to solar irradiance, a standard solar irradiance condition needs to be defined. The standard test condition (STC) prevailing in the industry is defined as

(1) Atmospheric mass (Air mass) AM1.5.

(2) Solar Irradiance (Solar Irradiance) $P = 1000\,\mathrm{W/m^2}$.

(3) Ambient temperature $T_a = 25 \pm 1°C$.

Through statistical records of the energy shown in Table 2: in general, the solar cell is also relatively larger, resulting in a larger open-circuit voltage, while a large band gap makes it more difficult for electrons, and vice versa.

The FF is an artificially specified parameter $FF = (V_{\max} \times J_{\max}/V_{oc} \times J_{sc})$, which is the maximum output power divided by the maximum current and voltage that the device can provide.

And for obtaining the value of R_s, R_{sh} in the analog circuit, we can obtain it by fitting the J – V curve of the device. From this we can obtain the following relationship:

$$J_{sh} = \frac{V_{sh}}{R_{sh}}. \tag{5}$$

$$J = J_{sc} - J_{\mathrm{dark}} - J_{sh.} \tag{6}$$

$$V_{sh} = V + JR_{s.} \tag{7}$$

Through the Shockley equation,

$$J_{\mathrm{dark}}(V) = J_0\left(\exp\left(\frac{qV}{k_BT}\right) - 1\right). \tag{8}$$

The dark state current density J_{dark}, where J_0 is the reverse saturation current density that can be obtained by performing a dark state $J - V$ curve test on the device.

Substituting equations (5), (7), and (8) into (6), we get

$$\mathrm{J}(V) = J_{sc} - J_0\left(\exp\left(\frac{q(V + J(V)R_s)}{k_BT}\right) - 1\right) - \frac{V + J(V)R_s}{R_{sh}}. \tag{9}$$

The value of R_s, R_{sh} for the device is obtained by fitting the $J - V$ curve of the device with equation (9).

4. Experiments

The reagents and materials used for the preparation of CdSeTe QDs included oleylamine (OAm, 80%–90%) and anhydrous methanol (CH_3OH), anhydrous ethanol (CH_3CH_2OH), acetone (CH_3COCH_3), dichloromethane(CH_2CI_2)), and trichloromethane ($CHCI_3$). The transparent electrodes for QDSCs were conductive glass (FTO, 14 Ω/square) purchased from Pilkington.

Scanning electron microscope (SEM) testing is a test method that uses the interaction between an electron beam and a material to analyze the morphology of the material surface. The SEM test mainly detects the secondary electron signal generated by the excitation of the material after the surface is bombarded by the electron beam. The SEM test equipment used in this work is a Shimadzu JSM-6700F scanning electron microscope.

4.1. Characterization Analysis Based on Cu_2SnS_3 Quantum Dot Material. We prepared Cu_2SnS_3 quantum dots by the thermal injection method, dissolved them in tetrachloroethylene solution, and then spin-coated them on the chalcogenide absorbing layer under nitrogen atmosphere after ultrasonic stirring and homogenization. It was reported that the reactivity of the precursor and the binding strength of the encapsulant had a great influence on the crystal structure of Cu_2SnS_3. By changing the reactivity of the precursor and/or the binding strength of the encapsulant, certain high-temperature and substable phases of the material can be obtained by wet chemistry at low temperatures, such that sphalerite structures, fibrillated zinc structures, and mixtures of sphalerite and fibrillated zinc structures can be obtained under different conditions. In this experiment, Cu_2SnS_3 quantum dots with sphalerite and fibrillar zincite structures were synthesized by wet chemistry at low temperature, and their structures are shown schematically in Figure 6.

In order to further determine the structure of the prepared Cu_2SnS_3 quantum dots, X-ray diffraction (XRD) analysis was performed to characterize them. Figure 7 shows the X-ray diffraction pattern of Cu_2SnS_3 quantum dots. The results show that we can prepare Cu_2SnS_3 quantum dots with sphalerite and sillimanite structures, respectively, and our diffraction patterns are consistent with the simulated and experimental patterns reported in the relevant literature.

As shown in Figure 8, in order to further determine the ratio of each element in the prepared Cu_2SnS_3 quantum dots and to avoid the formation of impurity phases such as Cu_3SnS_4, Cu_4SnS_4, and $Cu_2Sn_2S_7$, we performed energy dispersive spectroscopy (EDS) analysis on the Cu_2SnS_3 quantum dot films. The ratios of Cu, Sn, and S are basically

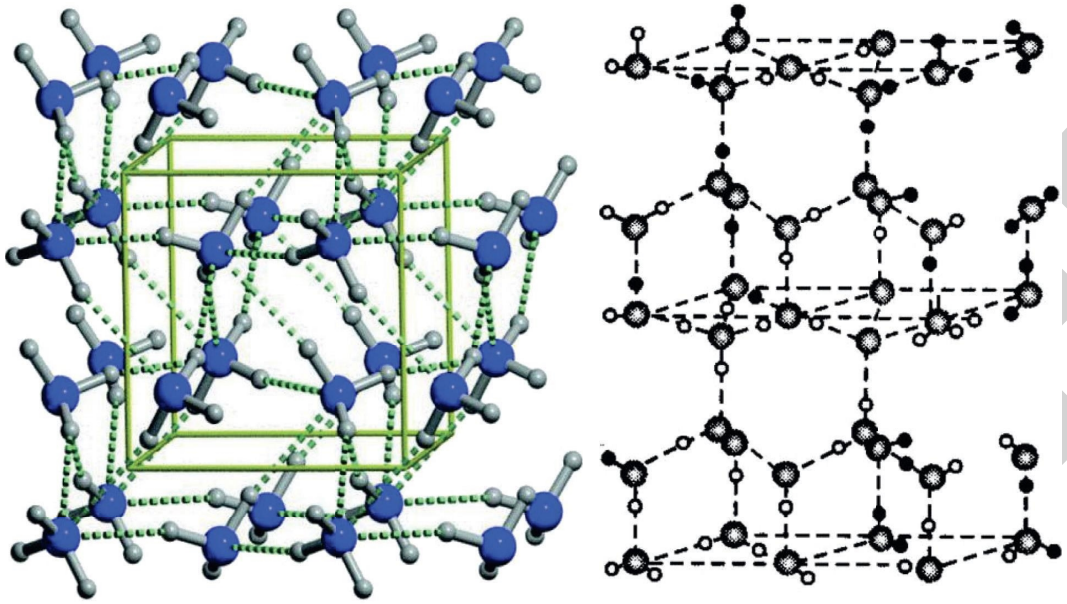

Figure 6: Schematic structure of sphalerite and sillimanite of Cu_2SnS_3 quantum dots.

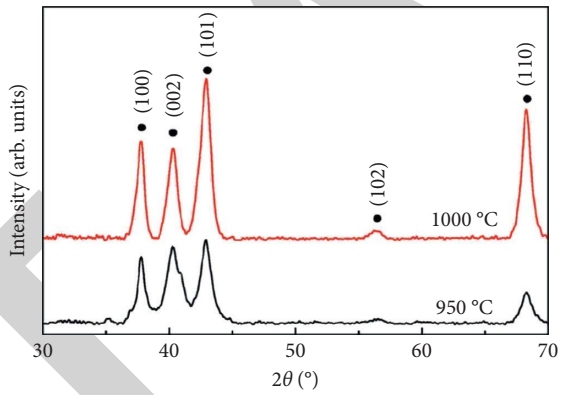

Figure 7: XRD patterns of sphalerite and fibrillar zincite structures of Cu_2SnS_3.

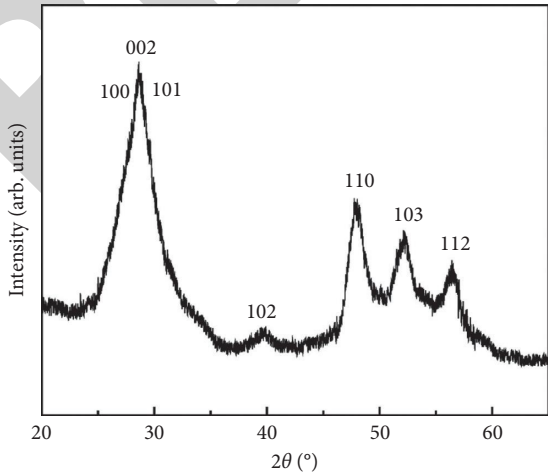

(a)

Element	Wt%	At%
SK	27.62	49.17
SnL	34.02	16.36
CuK	38.37	34.47
Matrix	Correction	ZAF

(b)

Figure 8: (a) EDS spectra of Cu_2SnS_3 quantum dots and (b) proportion of each element of Cu_2SnS_3 quantum dots measured by EDS.

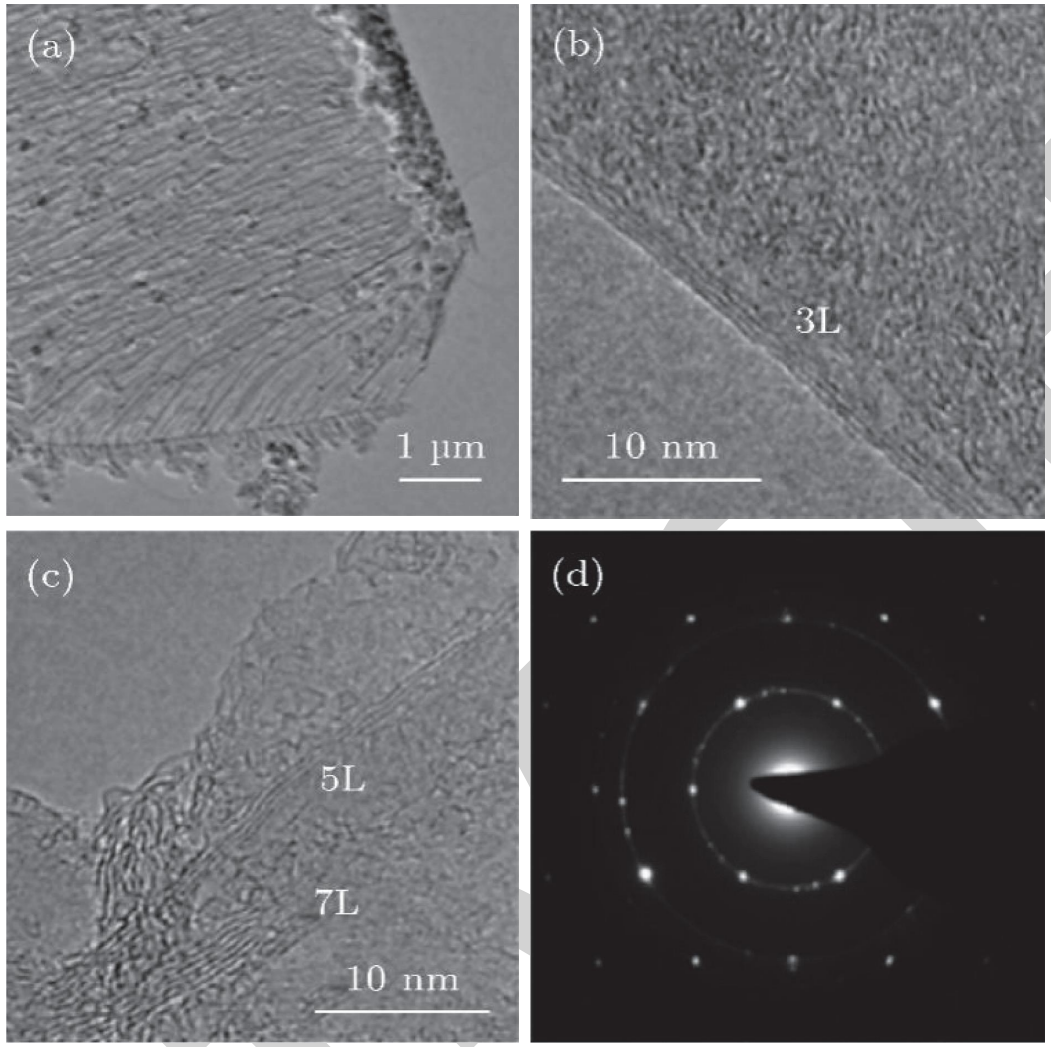

Figure 9: TEM images of Cu_2SnS_3 quantum dots at different magnifications: (a) 50,000x; (b) 80,000x; (c) 100,000x; (d) 150,000x.

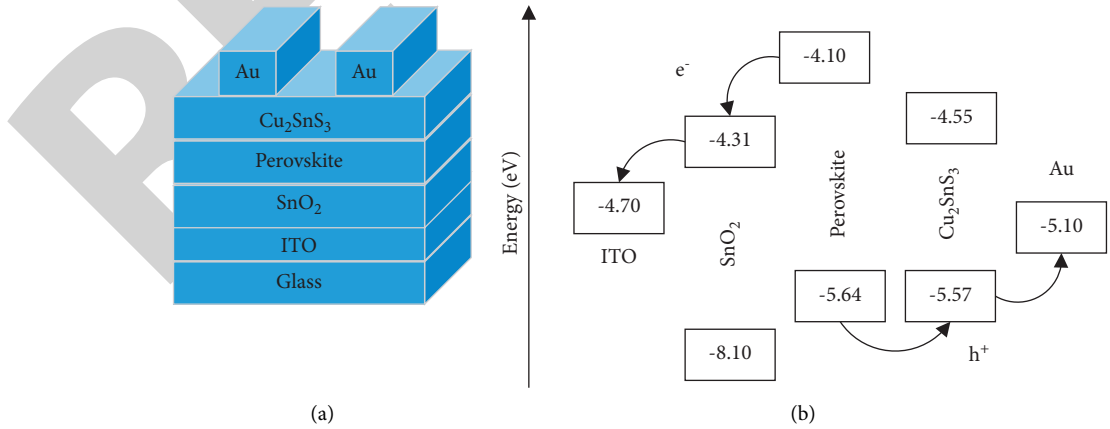

Figure 10: (a) Schematic diagram of the device structure of the prepared PSCs. (b) Energy band arrangement of each material in the prepared PSCs.

Table 3: $J-V$ test parameters of InN ultra-thin layer batteries grown at different temperatures.

Samples	J_{SC}/(mA/m^2)	V_{OC}/V	FF/%	n/%
Reference	13.27	0.55	62.36	4.67
InN-170°C	13.34	0.59	67.99	5.24
InN-200°C	14.44	0.59	69.99	5.48
InN-230°C	13.58	0.56	66.54	4.67

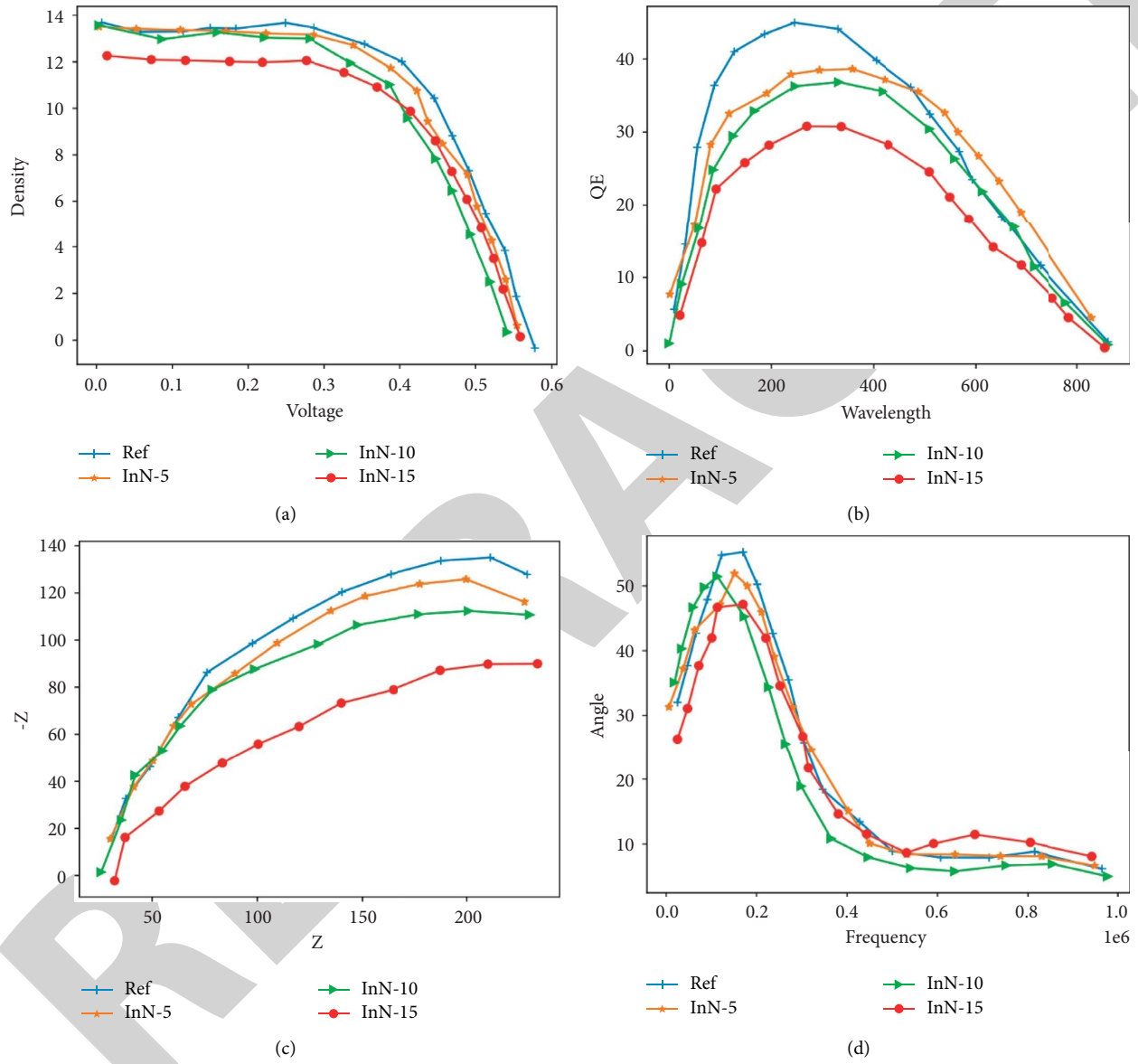

Figure 11: (a)$J-V$ curves of QDSCs based on different InN thickness; (b) quantum efficiency of QDSCs based on different thickness of InN; (c) Nyquist curves of QDSCs based on different thicknesses of InN; (d) bode curves of QDSCs based on different thicknesses of InN.

close to Cu : Sn : S = 2 : 1 : 3, which is consistent with the stoichiometric ratios of the quantum dots we prepared.

In order to better observe the morphology and size of the prepared quantum dots, transmission electron microscopy (TEM) characterization of Cu_2SnS_3 quantum dots was carried out. The TEM images of Cu_2SnS_3 quantum dots at different magnifications are shown in Figure 9. Based on the TEM images, it was found that the Cu_2SnS_3 quantum dots prepared by us have good dispersion ability, the size distribution is in the range of about 2–10 nm, and the morphology is mainly irregular polygons. The morphology and size of Cu_2SnS_3 quantum dots are mainly influenced by the reaction temperature and reaction time of the solution. The specific characteristics of Cu_2SnS_3 quantum dots are described in detail in the following section on the structural characterization of PSCs. The specific characteristics of

Cu_2SnS_3 quantum dot films are described in the next section on structural characterization of PSCs.

4.2. Device Film Characterization Based on Cu_2SnS_3 Hole Transport Material. Based on the preliminary research and characterization of the prepared Cu_2SnS_3 quantum dots, we believe that Cu_2SnS_3 quantum dots can be applied as HTM in PSCs. So we prepared the structure shown in Figure 10(a), in which SnO_2 is used as the ETM, Cu_2SnS_3 is used as the HTM, and the material used for the chalcogenide absorber layer is $(FAPbI_3)_{1-X}(MAPbBr_3)_X$. As shown in Figure 10 that the energy level diagram of each material shown in Figure 10(b) further demonstrates the degree of bandgap matching for each transmission layer of the prepared chalcogenide devices. After reviewing the literature, the conduction band position of ITO is −4.7 eV, the conduction band (Ec) and valence band (Ev) positions of SnO_2. As shown in Figure 10(b), the correlation between the band gaps of the layers is more intuitively demonstrated. The valence band value of Cu_2SnS_3 layer indicates that Cu_2SnS_3 quantum dots can replace Spiro-OMeTAD, effectively extract the holes generated by the chalcogenide layer.

The calculated *FF* is 69.98%. The *FF* is calculated as

$$\mathrm{FF} = \frac{P_m}{J_{sc}V_{oc}}. \tag{10}$$

Comparing the reference cell with the cell deposited with InN film at 200°C, it can be seen from the parameters in Table 3 that J_{sc} increases from 13.28 mA/cm^2 to 14.43 mA/cm^2 with little change, V_{oc} increases from 0.56 V to 0.58 V with little change; while *FF* increases from 62.37% to 69.98% with a large change.

To further investigate how the introduction of InN ultrathin layers affects the internal performance of the cell system of QDSCs, as shown in Figure 11 that the transport characteristics of electrons in the photoanodes of QDSCs are investigated in detail.

5. Conclusion

The photovoltaic performance of CdSeTe-based QDSCs can be enhanced to a certain extent by depositing InN ultra-thin layers using PEALD, and different deposition temperatures and thicknesses of InN show different influence patterns. The conversion efficiency of CdSeTe-based QDSCs was significantly improved by the introduction of InN ultra-thin layers in a certain thickness and deposition temperature range. Among them, the InN films at 200°C and 10 cycles are more ideal, and the conversion efficiency of the CdSeTe cells obtained can reach 5.47% and *FF* up to 69.98%. The introduction of InN can promote carrier transport, significantly increase *FF*, accelerate electron extraction, and reduce the transmission impedance $R_{ct-Tio2}$ at the photoanode.

Data Availability

The experimental data used to support the findings of this study are available from the corresponding author upon request.

Conflicts of Interest

The authors declared that they have no conflicts of interest regarding this work.

References

[1] N. Malek, N. Alias, S. Saad, N. A. Abdullah, and Y. Zhan, "Ultra-thin mos2 nanosheet for electron transport layer of perovskite solar cells," *Optical Materials*, vol. 104, Article ID 109933, 2020.

[2] S. Benabbas, Z. Rouabah, H. Heriche, and N. E. Chelali, "A numerical study of high efficiency ultra-thin cds/cigs solar cells," *African Journal of Science Technology Innovation & Development*, vol. 8, pp. 1–3, 2016.

[3] A. Sylla, N. Guessan Armel Ignace, T. Siaka, and J. P. Vilcot, "Theoretical analysis of the effect of the interfacial mose2 layer in cigs-based solar cells," *Open Journal of Modelling and Simulation*, vol. 9, no. 4, p. 12, 2021.

[4] K. Wang, C. Liu, C. Yi et al., "Efficient perovskite hybrid solar cells via ionomer interfacial engineering," *Advanced Functional Materials*, vol. 25, no. 44, pp. 6875–6884, 2016.

[5] Z. P. Li, S. Li, Y. Zheng et al., "The study of origin of interfacial perpendicular magnetic anisotropy in ultra-thin cofeb layer on the top of mgo based magnetic tunnel junction," *Applied Physics Letters*, vol. 109, no. 18, Article ID 12352, 2016.

[6] Q. Qin, Q. Shi, S. Wen, J. Wan, and Z. Hu, "Fabrication and interfacial electron transfer of ultrathin g-c3n4 nanosheet/tnt@cnts ternary nanostructure heterojunction for high-efficiency visible-light-driven photocatalysis," *Journal of Materials Science: Materials in Electronics*, vol. 29, no. 10, pp. 1–15, 2018.

[7] Q. Liu, C. Liu, and Y. Wang, "etc. Integrating external dictionary knowledge in conference scenarios the field of personalized machine translation method," *Journal of Chinese Informatics*, vol. 33, no. 10, pp. 31–37, 2019.

[8] P. An, Z. Wang, and C. Zhang, "Ensemble unsupervised autoencoders and Gaussian mixture model for cyberattack detection," *Information Processing & Management*, vol. 59, no. 2, Article ID 102844, 2022.

[9] R. Ali, M. Hameed Siddiqi, and S. Lee, "Rough set-based approaches for discretization: a compact review," *Artificial Intelligence Review*, vol. 44, no. 2, pp. 235–263, 2015.

[10] Y. Jia, H. Wang, Y. Wang, N. Shibayama, and H. Segawa, "High-performance electron-transport-layer-free quantum junction solar cells with improved efficiency exceeding 10%," *ACS Energy Letters*, vol. 6, no. 2, pp. 493–500, 2021.

[11] F. S. Shoyebmohamad, K. Hyeok-Chan, Y. Wooseok, and M. Jooho, "Performance enhancement of mesoporous tio 2-based perovskite solar cells by zns ultrathin-interfacial modification layer," *Journal of Alloys and Compounds: An Interdisciplinary Journal of Materials Science and Solid-state Chemistry and Physics*, vol. 738, pp. 405–414, 2018.

[12] E. Itoh, Y. Goto, Y. Saka, and K. Fukuda, "Interfacial energy alignment at the ito/ultra-thin electron selective dielectric layer interface and its effect on the efficiency of bulk-heterojunction organic solar cells," *Journal of Nanoscience and Nanotechnology*, vol. 16, no. 4, pp. 3248–3253, 2016.

[13] E. Etoh and M. Iwamoto, "Interfacial electrostatic phenomena and capacitance–voltage characteristics of ultrathin polyimide Langmuir–blodgett films," *Electrical Engineering in Japan*, vol. 134, no. 3, pp. 9–15, 2015.

[14] X. Zhang, Y. Li, R. Liu, Y. Rao, H. Rong, and G. Qin, "High-magnetization feco nanochains with ultrathin interfacial gaps

for broadband electromagnetic wave absorption at gigahertz," *ACS Applied Materials and Interfaces*, vol. 8, no. 5, pp. 3494–3498, 2016.

[15] G. Cai, Y. Fang, J. Wen, S. Mumtaz, Y. Song, and V. Frascolla, "Multi-carrier M-ary DCSK system with code index modulation: an efficient solution for chaotic communications," *IEEE Journal of Selected Topics in Signal Processing*, vol. 13, no. 6, pp. 1375–1386, 2019.

[16] K. Chandra, A. S. Marcano, S. Mumtaz, R. V. Prasad, and H. L. Christiansen, "Unveiling capacity gains in ultradense networks: using mm-wave NOMA," *IEEE Vehicular Technology Magazine*, vol. 13, no. 2, pp. 75–83, 2018.

[17] R. J. Yeo, N. Dwivedi, Z. Lu, Z. Zheng, and C. S. Bhatia, "Durable ultrathin silicon nitride/carbon bilayer overcoats for magnetic heads: the role of enhanced interfacial bonding," *Journal of Applied Physics*, vol. 117, no. 4, p. 1145, 2015.

[18] A. H. Kacha, M. N. Amroun, B. Akkal, and Z. Benamara, "Effect of the ultra-thin gan interlayer on the electrical and photoelectrical parameters of au|gaas Schottky barrier diodes," *Semiconductors*, vol. 55, no. 1, pp. S54–S61, 2022.

[19] C. Liu, H. Lü, T. Yang et al., "Ultrathin zno interfacial passivation layer for atomic layer deposited zro2 dielectric on the p-in0.2ga0.8as substrate," *Applied Surface Science*, vol. 444, no. 30, pp. 474–479, 2018.

[20] P. Vudumula and S. Kotamraju, "Improved device characteristics obtained in 4h-sic mosfet using high-k dielectric stack with ultrathin sio2-aln as interfacial layers," *Materials Science in Semiconductor Processing*, vol. 80, pp. 24–30, 2018.